

s_{\pm} pairing via interlayer interaction in $\text{La}_{2.85}\text{Pr}_{0.15}\text{Ni}_2\text{O}_7$ Thin Films under Ambient Pressure

Junkang Huang¹ and Tao Zhou^{1,2*}

¹*Guangdong Basic Research Center of Excellence for Structure and Fundamental Interactions of Matter, Guangdong Provincial Key Laboratory of Quantum Engineering and Quantum Materials, School of Physics, South China Normal University, Guangzhou 510006, China*

²*Guangdong-Hong Kong Joint Laboratory of Quantum Matter, Frontier Research Institute for Physics, South China Normal University, Guangzhou 510006, China*

(Dated: April 1, 2025)

We demonstrate that interlayer s_{\pm} -wave pairing dominates superconductivity in $\text{La}_{2.85}\text{Pr}_{0.15}\text{Ni}_2\text{O}_7$ thin films through self-consistent mean-field calculations. We further show that applying a perpendicular electric field breaks layer equivalence, generating nodal structures, Fermi arcs, and finite low-energy states in the $d_{x^2-y^2}$ orbital. Our results quantitatively align with recent experimental observations for the superconducting gaps, and we propose experimental symmetry-breaking perturbations as a direct test for the interlayer pairing mechanism.

A groundbreaking advancement in superconductivity research emerged with the discovery of high-temperature superconductivity in pressurized bilayer Ruddlesden-Popper nickelate $\text{La}_3\text{Ni}_2\text{O}_7$, exhibiting a superconducting transition temperature (T_c) of up to 80 K [1]. This milestone has ignited intense experimental and theoretical interest in nickel-based oxide superconductors, establishing them as a compelling platform for probing high-temperature superconductivity mechanisms [2–32]. Over the past year, analogous bilayer nickelate systems have demonstrated similarly remarkable properties: $\text{La}_2\text{PrNi}_2\text{O}_7$ was found to superconduct at 82.5 K [33], while $\text{La}_2\text{SmNi}_2\text{O}_{7-\delta}$ achieved an even higher- T_c of 91 K under pressure [34]. Notably, however, all these materials require external pressure to stabilize their superconducting states.

Recent breakthroughs have addressed this constraint by achieving ambient-pressure superconductivity in epitaxially stabilized thin-film nickelates. Specifically, $\text{La}_3\text{Ni}_2\text{O}_7$ and $\text{La}_{2.85}\text{Pr}_{0.15}\text{Ni}_2\text{O}_7$ thin films have shown superconducting transitions exceeding 40 K under ambient conditions [35, 36]. These advances mark pivotal progress toward practical applications, effectively bridging the gap between high-pressure bulk systems and ambient-pressure superconducting technologies.

Theoretical and experimental studies on $\text{La}_3\text{Ni}_2\text{O}_7$ and $\text{La}_{2.85}\text{Pr}_{0.15}\text{Ni}_2\text{O}_7$ thin-film superconductors reveal strong structural and electronic similarities with bilayer nickel-based bulk superconductors [35–43]. Both systems have tetragonal NiO_2 planes and a nearly linear apical Ni-O-Ni bond angle, which may be a critical feature for their superconducting properties [35, 36]. Density functional theory (DFT) calculations further demonstrate that electronic states near the Fermi level in the thin films are primarily governed by $\text{Ni-}d_{x^2-y^2}$ and $\text{Ni-}d_{z^2}$ orbitals [39, 43], consistent with bulk ones [8]. Angle-resolved photoemission spectroscopy

(ARPES) measurements of $\text{La}_{2.85}\text{Pr}_{0.15}\text{Ni}_2\text{O}_7$ thin films in the normal state show Fermi surface characteristics that align qualitatively with bulk materials [40]. Notably, recent ARPES investigations of the superconducting state in $\text{La}_{2.85}\text{Pr}_{0.15}\text{Ni}_2\text{O}_7$ reveal a nodeless superconducting gap, with the gap magnitude reaching its minimum along the diagonal direction [38]. This represents the first direct observation of the superconducting gap in bilayer nickel-based superconductors, offering key insights into their pairing mechanisms.

The Ruddlesden-Popper nickelate superconductor distinguishes itself from other unconventional high-temperature superconductors through the unique contribution of d_{z^2} orbital electrons to its Fermi surface [8, 39, 43]. This orbital, proposed to play a key role in superconductivity [1, 31, 32], mediates interlayer antiferromagnetic interactions that may promote interlayer electron pairing [18–26]. In this Letter, we employ a two-orbital model tailored to $\text{La}_{2.85}\text{Pr}_{0.15}\text{Ni}_2\text{O}_7$ thin films and perform self-consistent mean-field calculations to investigate superconducting pairing mechanism. By incorporating both interlayer and intralayer electron interactions, our results reveal that interlayer pairing dominates, yielding an effective s_{\pm} symmetry. Furthermore, we demonstrate how perpendicular electric fields modulate the pairing function, providing a useful experimental signature for probing interlayer pairing. These findings provide theoretical guidance for experimental efforts aimed at verifying the predominance of interlayer pairing mechanisms in this material class.

We consider a Hamiltonian that incorporates both tight-binding terms and interaction terms, expressed as follows:

$$H = \sum_{l,l'} \sum_{i,j,\tau,\tau',\sigma} t_{ij\tau\tau'}^{l,l'} c_{i\tau\sigma}^{l\dagger} c_{j\tau'\sigma}^{l'} + \sum_{l,i,\tau,\sigma} \varepsilon_l n_{i\tau\sigma}^l + H_I, \quad (1)$$

where l/l' , τ/τ' , and σ denote the layer, orbital, and spin indices, respectively. The particle number operator is defined as $n_{i\tau\sigma}^l = c_{i\tau\sigma}^{l\dagger} c_{i\tau\sigma}^l$. The layer-dependent onsite energy ε_l is introduced to account for the effects of an external perpendicular electric field.

* tzhou@scnu.edu.cn

The tight-binding parameters are adapted from Ref. [39] and adjusted to match experimental observations. Specifically, we have judiciously increased the interlayer hopping constant of the d_{z^2} orbital to align with the Fermi surface reported in ARPES experiments [40]. The complete set of tight-binding parameters is provided in the supplemental material [44].

The interaction term is given by:

$$H_I = - \sum_{l,l'} \sum_{i,j,\tau} V_{ij\tau}^{l,l'} \left(n_{i\tau\uparrow}^l n_{j\tau\downarrow}^{l'} + n_{i\tau\downarrow}^l n_{j\tau\uparrow}^{l'} \right). \quad (2)$$

At the mean-field level, the intralayer pairing order parameter is defined as $\Delta_{ij\parallel}^{l\tau} = \frac{V_{ij\parallel}^\tau}{2} \langle c_{i\tau\uparrow}^l c_{j\tau\downarrow}^l - c_{i\tau\downarrow}^l c_{j\tau\uparrow}^l \rangle$, where i and j denote nearest neighbor sites within the same layer. For interlayer pairing, the interlayer interaction strength is given by $V_{\perp}^\tau = V_{ii\tau}^{l,l'}$, and the corresponding mean-field order parameter is $\Delta_{i\perp}^\tau = \frac{V_{\perp}^\tau}{2} \langle c_{i\tau\uparrow}^l c_{i\tau\downarrow}^{l'} - c_{i\tau\downarrow}^l c_{i\tau\uparrow}^{l'} \rangle$.

The Hamiltonian can be transformed into momentum space via a Fourier transformation, resulting in the expression $H = \sum_{\mathbf{k}} \Psi^\dagger(\mathbf{k}) \hat{M}(\mathbf{k}) \Psi(\mathbf{k})$. Here, \hat{M} is an 8×8 matrix [44], and the Nambu spinor $\Psi(\mathbf{k})$ is defined as $\Psi(\mathbf{k}) = (u_{\mathbf{k}}, v_{\mathbf{k}})^T$, where $u_{\mathbf{k}} = (c_{\mathbf{k}x\uparrow}^1, c_{\mathbf{k}z\uparrow}^1, c_{\mathbf{k}x\uparrow}^2, c_{\mathbf{k}z\uparrow}^2)$, and $v_{\mathbf{k}} = (c_{-\mathbf{k}x\downarrow}^{1\dagger}, c_{-\mathbf{k}z\downarrow}^{1\dagger}, c_{-\mathbf{k}x\downarrow}^{2\dagger}, c_{-\mathbf{k}z\downarrow}^{2\dagger})$.

The intralayer and interlayer pairing order parameters can be determined by

$$\Delta_{\parallel}^{l\tau} = \frac{1}{4N} \sum_{n\mathbf{k}} V_{\parallel}^\tau u_{nl\tau} v_{nl\tau}^* \tanh\left(\frac{\beta E_{n\mathbf{k}}}{2}\right) (\cos \mathbf{k}_x + \cos \mathbf{k}_y),$$

$$\Delta_{\perp}^\tau = \frac{1}{2N} \sum_{n\mathbf{k}} V_{\perp}^\tau u_{nl\tau} v_{nl\tau}^* \tanh\left(\frac{\beta E_{n\mathbf{k}}}{2}\right).$$

The Green's function matrix is defined as:

$$G_{ij}(\mathbf{k}, \omega) = \sum_n \frac{u_{in}(\mathbf{k}) u_{jn}^*(\mathbf{k})}{\omega - E_n(\mathbf{k}) + i\Gamma}, \quad (5)$$

where Γ is a damping factor, set to $\Gamma = 0.002$.

The spectral function of layer l and orbital τ is expressed as:

$$A_\tau^l(\mathbf{k}, \omega) = -\frac{1}{\pi} \text{Im} [G_{pp}(\mathbf{k}, \omega) + G_{p+4,p+4}(\mathbf{k}, -\omega)], \quad (6)$$

with $p = \tau + 2(l - 1)$, where l and τ take values 1 or 2.

The density of states (DOS) is represented as a function of frequency through integration of the spectral function over all momenta:

$$\rho_\tau^l(\omega) = \frac{1}{N} \sum_{\mathbf{k}} A_\tau^l(\mathbf{k}, \omega). \quad (7)$$

Our investigation commences with an exploration of the pairing mechanism of Ruddlesden-Popper nickelate superconductor. The superconducting pairing strength V

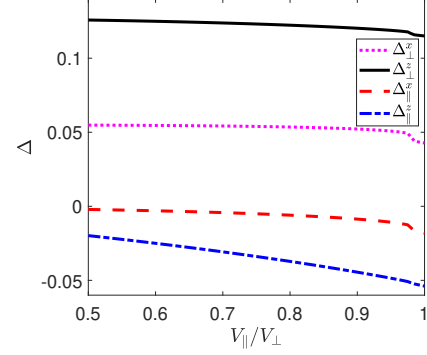


FIG. 1. Variation of order parameters as a function of intralayer pairing strength V_{\parallel} , ranging from 0.4 to 0.8, with interlayer pairing strength fixed at $V_{\perp} = 0.8$.

is determined by the superexchange interactions J , with $J \approx 4t^2/U$. Therefore, it is widely accepted that the pairing strength V is proportional to the square of the corresponding hopping constant, expressed as $V \propto t^2$. In our model, the most dominant hopping constant is the interlayer hopping constant for the $d_{3z^2-r^2}$ ($|t_{\perp}^z| = 0.670$), and the second dominant is the intralayer nearest-neighbor hopping constant for the $d_{x^2-y^2}$ orbital ($|t_{\parallel}^x| = 0.466$). Several studies have highlighted the significant role of Hund's coupling between the $d_{x^2-y^2}$ and d_{z^2} orbitals in enhancing superconducting pairing [14–18]. Specifically, due to the plentiful Hund's coupling, d_{z^2} orbital and $d_{x^2-y^2}$ orbital can effectively share pairing strength each other [14–18]. Consequently, in the following presented results, the pairing interaction for the $d_{x^2-y^2}$ and d_{z^2} orbitals are treated equally with $V_{\parallel}^x = V_{\parallel}^z = V_{\parallel}$ and $V_{\perp}^x = V_{\perp}^z = V_{\perp}$.

To investigate the role of intralayer pairing, we have conducted a detailed study that the interlayer pairing strengths are fitted and set to $V_{\perp} = 0.8$, while the intralayer pairing strengths V_{\parallel} increases from 0.4 to 0.8. The self-consistent results are shown in Fig. 1. Within the current parameter range, our results demonstrate that interlayer pairing is dominant. As the intralayer pairing potential increases, the amplitude of the intralayer s -wave pairing order parameter correspondingly increases, while the interlayer order parameter remains at a relatively high level. When the intralayer pairing potential equals the interlayer pairing potential, the largest pairing order parameter is still the interlayer pairing of the d_{z^2} orbital, whereas the intralayer pairing of the $d_{x^2-y^2}$ orbital remains negligible. Additionally, it is noteworthy that the pairing signs of the intralayer and interlayer order parameters are always opposite.

We now explore the effective pairing information along the Fermi surface pockets. The pairing function in the orbital basis can be transformed to the band basis with $\hat{\Delta}_{\mathbf{k}} = \Psi_0^\dagger(\mathbf{k}) \Delta_{\mathbf{k}} \Psi_0(\mathbf{k})$, where $\Psi_0(\mathbf{k})$ denotes the eigenvector matrix of the normal-state Hamiltonian, and $\Delta_{\mathbf{k}}$ represents the matrix form of the pairing term in the

Hamiltonian [44]. The four diagonal components of the pairing function matrix $\hat{\Delta}_{\mathbf{k}}$ are corresponding to the intraband pairings of the four normal-state bands, respectively.

Based on mean-field self-consistent results shown in Fig. 1, the intralayer $d_{x^2-y^2}$ -wave pairing order parameter is negligible, prompting a focus on purely interlayer pairing—a configuration supported by several theoretical studies [18–26]. We also explore a hybrid state combining interlayer and intralayer pairing, where interlayer pairing remains dominant, as indicated by mean-field calculations. Numerical calculations of the pairing order parameters along the normal-state Fermi surface are shown in Figs. 2(a) and 2(b) for interaction configurations $(V_{\perp}, V_{\parallel}) = (0.8, 0)$ (solely interlayer coupling) and $(V_{\perp}, V_{\parallel}) = (0.8, 0.6)$ (mixed interlayer-intralayer coupling), respectively. As is seen, for both configurations, an effective s_{\pm} pairing symmetry is revealed, with the pairing order parameter is positive along γ and α Fermi pockets and negative along β one. This typical s_{\pm} pairing symmetry is consistent with previous theoretically obtained s_{\pm} pairing symmetry based on the spin fluctuation scenario [9–13].

We present the numerical results of the energy gap magnitudes along the the three Fermi pockets with these two configures in Figs. 2(c) and 2(d), respectively. When only interlayer electron pairing is considered, as shown in Fig. 2(c), the superconducting gap is nodeless along all three Fermi pockets. Along the γ Fermi pocket, the gap remains constant ($\Delta_{\gamma} = 0.13$). For the α and β Fermi pockets, the gap is anisotropic, reaching a minimum along the diagonal direction ($\theta = 0$) and increasing monotonically with θ . This aligns with recent ARPES experimental results on the gap magnitude near the diagonal direction [38]. When both interlayer and intralayer electron pairing are present, as depicted in Fig. 2(d), the gap magnitude along the γ Fermi pocket increases significantly ($\Delta_{\gamma} \approx 0.21$). This is due to the intralayer order parameter having a negative sign [Fig. 1], while the γ Fermi pocket is near the M point with $M = (\pi, \pi)$, where the intralayer pairing generates a positive effective pairing order parameter that combines with the original interlayer one. The gap behavior along the α and β Fermi surfaces differs greatly from the solely interlayer-pairing case. Along the α pocket, the gap decreases slightly with increasing θ . Along the β pocket, the gap exhibits non-monotonic behavior, first increasing and then decreasing with θ .

We further examine the impact of the intralayer pairing component on the superconducting gap magnitude of the α and β Fermi pockets. Figs. 2(e) and 2(f) show the θ -dependence of the gap along the α and β pockets, respectively, with the intralayer interaction V_{\parallel} increasing from 0 to 0.6. Along the α pocket [Fig. 2(e)], the gap increases monotonically with θ when $V_{\parallel} < 0.5$ but decreases monotonically when $V_{\parallel} > 0.5$. For the β pocket [Fig. 2(d)], the gap magnitude exhibits pronounced variations near the diagonal direction as V_{\parallel} increases. Notably, when

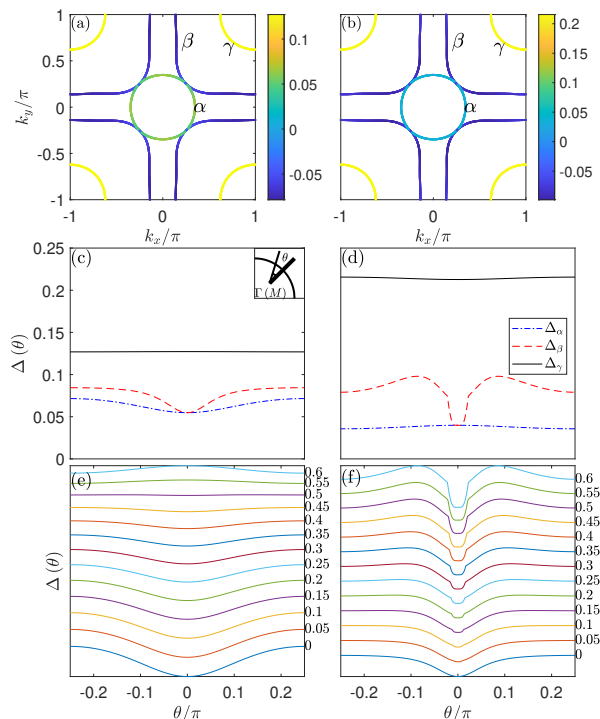


FIG. 2. (a) Gap function projected onto the Fermi surface with only interlayer pairing considered. (b) Similar to panel (a), but with coexistence of interlayer and intralayer pairing. (c) Magnitudes of the energy gap along different Fermi pockets with only interlayer pairing considered. (d) Similar to panel (c), but with coexistence of interlayer and intralayer pairing. (e) Magnitudes of the energy gap along the α Fermi pocket with the intralayer pairing strength V_{\parallel} increasing from 0 to 0.6. (d) Similar to panel (e), but for the β Fermi pocket.

$V_{\parallel} > 0.25$, the gap develops non-monotonic behavior, first increasing and then decreasing with θ . These gap variations can be detected in future experiments to determine the weight of the intralayer pairing component.

Our calculations demonstrate that interlayer pairing alone yields results qualitatively consistent with experimental observations in nickelate superconductors [38]. Notably, prior work on the trilayer nickelate $\text{La}_4\text{Ni}_3\text{O}_{10}$ underscores the potential for interlayer pairing to produce nodes or nodal lines in the superconducting order parameter [45, 46]. This nodal structure stems from the intrinsic electronic inequivalence between the inner and outer NiO_2 layers in the trilayer geometry. In contrast, bilayer nickelate superconductors feature two electronically equivalent NiO_2 layers. As a result, interlayer Cooper pairing in such systems produces a nodeless superconducting order parameter due to the symmetry of the pairing wavefunction. However, if the equivalence between the two layers is experimentally disrupted, interlayer pairing could induce nodes or nodal lines, offering a critical test for the dominance of interlayer pairing in these materials.

Experimentally, layer equivalence can be broken in

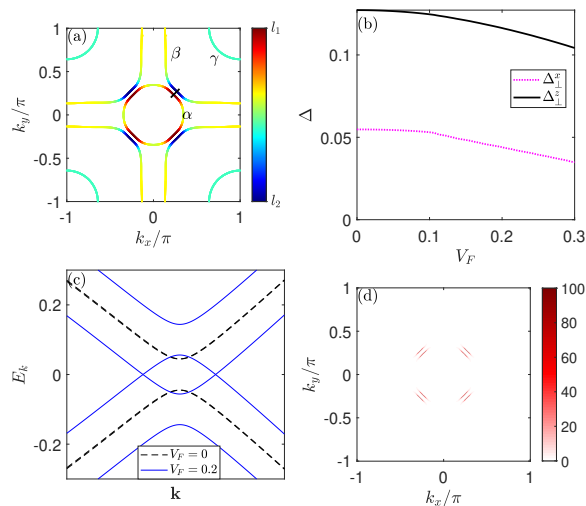


FIG. 3. (a) Normal-state Fermi surface with an applied interlayer voltage $V_F = 0.2$. (b) Self-consistent results of interlayer pairing order parameters as a function of voltage V_F . (c) Superconducting energy bands along the short line cut in panel (a), comparing $V_F = 0.0$ (black dashed lines) and $V_F = 0.2$ (blue solid lines). (d) Zero-energy spectral function in the superconducting state with $V_F = 0.2$.

thin-film bilayers by applying a perpendicular electric field [27] or inserting ionic spacer layers between unit cells [47–49]. Theoretically, this corresponds to introducing a layer-dependent chemical potential term in Eq.(1) with $\varepsilon_l = \frac{(-1)^l V_F}{2}$ (V_F is the interlayer voltage), which explicitly breaks the equivalence of the two layers. Observing nodal features under such asymmetry would confirm that interlayer pairing governs superconductivity in bilayer nickelates.

We replot the normal state Fermi surface in the presence of additional effective perpendicular field with $V_F = 0.2$ in Fig. 3(a). As is shown, the application of a perpendicular electric field induces significant modifications to the α and β Fermi pockets near the diagonal direction. In the absence of the field, these pockets are adjacent along the diagonal. Under the electric field, however, the α and β pockets separate. Near the diagonal, the α pocket is dominated by quasiparticles from layer 1, while the β pocket primarily originates from layer 2. Within the interlayer pairing framework, this layer-dependent separation suppresses quasiparticle pairing near the diagonal, predicting the emergence of additional nodal regions in the superconducting state.

In Fig. 3(b), we show self-consistent calculations of the interlayer pairing order parameters with different voltage V_F . For both orbitals the interlayer pairing order parameter decreases with increasing V_F , consistent with the broken equivalence between the two NiO_2 layers. Notably, even under a strong field ($V_F = 0.3$), the interlayer pairing in the d_{z^2} orbital retains a relatively large value (about 0.1).

Fig. 3(c) displays the energy bands in the supercon-

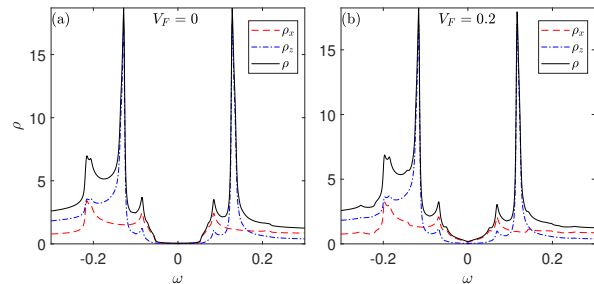


FIG. 4. DOS spectra in the superconducting state with (a) $V_F = 0$ and (b) $V_F = 0.2$.

ducting state near the α and β Fermi pockets along the diagonal direction (along the short line in Fig. 3(a)). At $V_F = 0$, the α and β bands are degenerate and exhibit a full superconducting gap. When $V_F = 0.2$, however, the bands split, generating two nodes at the α and β Fermi pockets, respectively. Fig. 3(d) illustrates the zero-energy spectral function of the superconducting state at $V_F = 0.2$, revealing two disconnected Fermi arcs. These arcs arise from the two electronically inequivalent NiO_2 layers, which cannot form Cooper pairs due to their electronic inequivalence [see Fig. 3(a)]. The arc size depends sensitively on V_F . Our calculations show that the arcs first emerge at $V_F = 0.11$ and grow progressively with increasing V_F [44].

Finally, we analyze the modifications to the DOS spectrum induced by an external electric field. Fig. 4 compares the calculated DOS for field-free and field-applied configurations. In the absence of an external electric field ($V_F = 0$), the system is fully gapped, with the $d_{x^2-y^2}$ and d_{z^2} orbitals displaying U-shaped spectral profiles. The coherent peak of the d_{z^2} orbital occurs at higher energies with enhanced intensity.

When an external electric field is applied ($V_F = 0.2$), the energy gap of the d_{z^2} orbital narrows, though its DOS remains vanishingly small near the Fermi level. In contrast, the $d_{x^2-y^2}$ orbital develops finite low-energy states, signaling the presence of unpaired quasiparticles. These results align with the nodal structure observed in the superconducting state (see Fig. 3), further corroborating the interplay between electronic asymmetry and gap modulation under external fields.

In summary, our study establishes that interlayer pairing serves as the dominant mechanism underpinning superconductivity in $\text{La}_{2.85}\text{Pr}_{0.15}\text{Ni}_2\text{O}_7$ thin films, yielding an effective s_{\pm} gap symmetry consistent with experimental evidence of nodeless superconducting gaps. We further demonstrate that a perpendicular electric field disrupts the equivalence between NiO_2 layers, inducing the emergence of nodal gap structures, Fermi arcs, and finite low-energy states in the $d_{x^2-y^2}$ orbital channel. These results not only deepen the understanding of superconductivity in nickelates but also suggest experimental protocols to confirm the interlayer pairing paradigm through detection of nodal features or discontinuous Fermi arcs

under external perturbations. Moreover, our findings reveal an unprecedented pathway for electric-field engineer-

ing of superconducting states, thereby paving the way for exploring exotic quantum phases via layer-selective external fields or symmetry-breaking modifications.

-
- [1] H. Sun, M. Huo, X. Hu, J. Li, Z. Liu, Y. Han, L. Tang, Z. Mao, P. Yang, B. Wang, J. Cheng, D.-X. Yao, G.-M. Zhang, and M. Wang, Signatures of superconductivity near 80K in a nickelate under high pressure, *Nature* **621**, 493 (2023).
- [2] M. Wang, H.-H. Wen, T. Wu, D.-X. Yao, and T. Xiang, Normal and superconducting properties of $\text{La}_3\text{Ni}_2\text{O}_7$, *Chin. Phys. Lett.* **41**, 077402 (2024).
- [3] Z. Liu, M. Huo, J. Li, Q. Li, Y. Liu, Y. Dai, X. Zhou, J. Hao, Y. Lu, M. Wang, and H.-H. Wen, Electronic correlations and partial gap in the bilayer nickelate $\text{La}_3\text{Ni}_2\text{O}_7$, *Nat. Commun.* **15**, 7570 (2024).
- [4] Y. Zhang, D. Su, Y. Huang, Z. Shan, H. Sun, M. Huo, K. Ye, J. Zhang, Z. Yang, Y. Xu, Y. Su, R. Li, M. Smidman, M. Wang, L. Jiao, and H. Yuan, High-temperature superconductivity with zero resistance and strange-metal behaviour in $\text{La}_3\text{Ni}_2\text{O}_7\delta$, *Nat. Phys.* **20**, 1269 (2024).
- [5] K. Chen, X. Liu, J. Jiao, M. Zou, C. Jiang, X. Li, Y. Luo, Q. Wu, N. Zhang, Y. Guo, and L. Shu, Evidence of spin density waves in $\text{La}_3\text{Ni}_2\text{O}_7-\delta$, *Phys. Rev. Lett.* **132**, 256503 (2024).
- [6] Z. Dong, M. Huo, J. Li, J. Li, P. Li, H. Sun, L. Gu, Y. Lu, M. Wang, Y. Wang, and Z. Chen, Visualization of oxygen vacancies and self-doped ligand holes in $\text{La}_3\text{Ni}_2\text{O}_7\delta$, *Nature* **630**, 847 (2024).
- [7] G. Wang, N. N. Wang, X. L. Shen, J. Hou, L. Ma, L. F. Shi, Z. A. Ren, Y. D. Gu, H. M. Ma, P. T. Yang, Z. Y. Liu, H. Z. Guo, J. P. Sun, G. M. Zhang, S. Calder, J.-Q. Yan, B. S. Wang, Y. Uwatoko, and J.-G. Cheng, Pressure-induced superconductivity in polycrystalline $\text{La}_3\text{Ni}_2\text{O}_7-\delta$, *Phys. Rev. X* **14**, 011040 (2024).
- [8] Z. Luo, X. Hu, M. Wang, W. Wú, and D.-X. Yao, Bilayer two-orbital model of $\text{La}_3\text{Ni}_2\text{O}_7$ under pressure, *Phys. Rev. Lett.* **131**, 126001 (2023).
- [9] Y.-B. Liu, J.-W. Mei, F. Ye, W.-Q. Chen, and F. Yang, s^\pm -wave pairing and the destructive role of apical-oxygen deficiencies in $\text{La}_3\text{Ni}_2\text{O}_7$ under pressure, *Phys. Rev. Lett.* **131**, 236002 (2023).
- [10] Y. Zhang, L.-F. Lin, A. Moreo, T. A. Maier, and E. Dagotto, Trends in electronic structures and s_\pm -wave pairing for the rare-earth series in bilayer nickelate superconductor $\text{R}_3\text{Ni}_2\text{O}_7$, *Phys. Rev. B* **108**, 165141 (2023).
- [11] Q.-G. Yang, D. Wang, and Q.-H. Wang, Possible s_\pm -wave superconductivity in $\text{La}_3\text{Ni}_2\text{O}_7$, *Phys. Rev. B* **108**, L140505 (2023).
- [12] K.-Y. Jiang, Y.-H. Cao, Q.-G. Yang, H.-Y. Lu, and Q.-H. Wang, Theory of pressure dependence of superconductivity in bilayer nickelate $\text{La}_3\text{Ni}_2\text{O}_7$, *Phys. Rev. Lett.* **134**, 076001 (2025).
- [13] W. Xi, S.-L. Yu, and J.-X. Li, Transition from s_\pm -wave to $d_{x^2-y^2}$ -wave superconductivity driven by interlayer interaction in the bilayer two-orbital model of $\text{La}_3\text{Ni}_2\text{O}_7$, *Phys. Rev. B* **111**, 104505 (2025).
- [14] C. Lu, Z. Pan, F. Yang, and C. Wu, Interplay of two E_g orbitals in superconducting $\text{La}_3\text{Ni}_2\text{O}_7$ under pressure, *Phys. Rev. B* **110**, 094509 (2024).
- [15] Y.-H. Tian, Y. Chen, J.-M. Wang, R.-Q. He, and Z.-Y. Lu, Correlation effects and concomitant two-orbital s_\pm -wave superconductivity in $\text{La}_3\text{Ni}_2\text{O}_7$ under high pressure, *Phys. Rev. B* **109**, 165154 (2024).
- [16] Y. Cao and Y.-f. Yang, Flat bands promoted by Hund's rule coupling in the candidate double-layer high-temperature superconductor $\text{La}_3\text{Ni}_2\text{O}_7$ under high pressure, *Phys. Rev. B* **109**, L081105 (2024).
- [17] X.-Z. Qu, D.-W. Qu, X.-W. Yi, W. Li, and G. Su, Hund's rule, interorbital hybridization, and high- T_c superconductivity in the bilayer nickelate (2025), [arXiv:2311.12769](https://arxiv.org/abs/2311.12769) [cond-mat.str-el].
- [18] H. Oh and Y.-H. Zhang, Type-II $t-j$ model and shared superexchange coupling from Hund's rule in superconducting $\text{La}_3\text{Ni}_2\text{O}_7$, *Phys. Rev. B* **108**, 174511 (2023).
- [19] T. Xie, M. Huo, X. Ni, F. Shen, X. Huang, H. Sun, H. C. Walker, D. Adroja, D. Yu, B. Shen, L. He, K. Cao, and M. Wang, Strong interlayer magnetic exchange coupling in $\text{La}_3\text{Ni}_2\text{O}_7-\delta$ revealed by inelastic neutron scattering, *Sci. Bull.* **69**, 3221 (2024).
- [20] X. Chen, J. Choi, Z. Jiang, J. Mei, K. Jiang, J. Li, S. Agrestini, M. Garcia-Fernandez, H. Sun, X. Huang, D. Shen, M. Wang, J. Hu, Y. Lu, K.-J. Zhou, and D. Feng, Electronic and magnetic excitations in $\text{La}_3\text{Ni}_2\text{O}_7$, *Nat. Commun.* **15**, 9597 (2024).
- [21] Y.-f. Yang, G.-M. Zhang, and F.-C. Zhang, Interlayer valence bonds and two-component theory for high- T_c superconductivity of $\text{La}_3\text{Ni}_2\text{O}_7$ under pressure, *Phys. Rev. B* **108**, L201108 (2023).
- [22] J. Chen, F. Yang, and W. Li, Orbital-selective superconductivity in the pressurized bilayer nickelate $\text{La}_3\text{Ni}_2\text{O}_7$: An infinite projected entangled-pair state study, *Phys. Rev. B* **110**, L041111 (2024).
- [23] C. Lu, Z. Pan, F. Yang, and C. Wu, Interlayer-coupling-driven high-temperature superconductivity in $\text{La}_3\text{Ni}_2\text{O}_7$ under pressure, *Phys. Rev. Lett.* **132**, 146002 (2024).
- [24] J.-R. Xue and F. Wang, Magnetism and superconductivity in the t - J model of $\text{La}_3\text{Ni}_2\text{O}_7$ under multiband gutzwiller approximation, *Chin. Phys. Lett.* **41**, 057403 (2024).
- [25] Y.-f. Yang, Decomposition of multilayer superconductivity with interlayer pairing, *Phys. Rev. B* **110**, 104507 (2024).
- [26] M. Lu and T. Zhou, Spin excitations in bilayer $\text{La}_3\text{Ni}_2\text{O}_7$ superconductors with interlayer pairing, *Phys. Rev. B* **111**, 094504 (2025).
- [27] Z.-Y. Shao, J.-H. Ji, C. Wu, D.-X. Yao, and F. Yang, Possible high-temperature superconductivity driven by perpendicular electric field in the $\text{La}_3\text{Ni}_2\text{O}_7$ single-bilayer film at ambient pressure (2024), [arXiv:2411.13554](https://arxiv.org/abs/2411.13554) [cond-mat.supr-con].
- [28] Y. Liu, M. Ou, H. Chu, H. Yang, Q. Li, Y.-J. Zhang, and H.-H. Wen, Growth and characterization of the $\text{La}_3\text{Ni}_2\text{O}_7-\delta$ thin films: Dominant contribution of the $d_{x^2-y^2}$ orbital at ambient pressure, *Phys. Rev. Mater.* **8**, 124801 (2024).

- [29] J. Huang, Z. D. Wang, and T. Zhou, Impurity and vortex states in the bilayer high-temperature superconductor $\text{La}_3\text{Ni}_2\text{O}_7$, *Phys. Rev. B* **108**, 174501 (2023).
- [30] Z. Fan, J.-F. Zhang, B. Zhan, D. Lv, X.-Y. Jiang, B. Normand, and T. Xiang, Superconductivity in nickelate and cuprate superconductors with strong bilayer coupling, *Phys. Rev. B* **110**, 024514 (2024).
- [31] Z. Huo, Z. Luo, P. Zhang, A. Yang, Z. Liu, X. Tao, Z. Zhang, S. Guo, Q. Jiang, W. Chen, D.-X. Yao, D. Duan, and T. Cui, Modulation of the octahedral structure and potential superconductivity of $\text{La}_3\text{Ni}_2\text{O}_7$ through strain engineering, *Sci. China: Phys., Mech. Astron.* **68**, 237411 (2025).
- [32] W. Wu, Z. Luo, D.-X. Yao, and M. Wang, Superexchange and charge transfer in the nickelate superconductor $\text{La}_3\text{Ni}_2\text{O}_7$ under pressure, *Sci. China Phys. Mech. Astron.* **67**, 117402 (2024).
- [33] N. Wang, G. Wang, X. Shen, J. Hou, J. Luo, X. Ma, H. Yang, L. Shi, J. Dou, J. Feng, J. Yang, Y. Shi, Z. Ren, H. Ma, P. Yang, Z. Liu, Y. Liu, H. Zhang, X. Dong, Y. Wang, K. Jiang, J. Hu, S. Nagasaki, K. Kitagawa, S. Calder, J. Yan, J. Sun, B. Wang, R. Zhou, Y. Uwatoko, and J. Cheng, Bulk high-temperature superconductivity in pressurized tetragonal $\text{La}_2\text{PrNi}_2\text{O}_7$, *Nature* **634**, 579 (2024).
- [34] F. Li, D. Peng, J. Dou, N. Guo, L. Ma, C. Liu, L. Wang, Y. Zhang, J. Luo, J. Yang, J. Zhang, W. Cai, J. Cheng, Q. Zheng, R. Zhou, Q. Zeng, X. Tao, and J. Zhang, Ambient pressure growth of bilayer nickelate single crystals with superconductivity over 90 K under high pressure (2025), [arXiv:2501.14584](https://arxiv.org/abs/2501.14584) [cond-mat.supr-con].
- [35] E. K. Ko, Y. Yu, Y. Liu, L. Bhatt, J. Li, V. Thampy, C.-T. Kuo, B. Y. Wang, Y. Lee, K. Lee, J.-S. Lee, B. H. Goodge, D. A. Muller, and H. Y. Hwang, Signatures of ambient pressure superconductivity in thin film $\text{La}_3\text{Ni}_2\text{O}_7$, *Nature* **638**, 935 (2025).
- [36] G. Zhou, W. Lv, H. Wang, Z. Nie, Y. Chen, Y. Li, H. Huang, W. Chen, Y. Sun, Q.-K. Xue, and Z. Chen, Ambient-pressure superconductivity onset above 40 K in $(\text{La},\text{Pr})_3\text{Ni}_2\text{O}_7$ films, *Nature* [10.1038/s41586-025-08755-z](https://doi.org/10.1038/s41586-025-08755-z) (2025).
- [37] Y. Liu, E. K. Ko, Y. Tarn, L. Bhatt, B. H. Goodge, D. A. Muller, S. Raghu, Y. Yu, and H. Y. Hwang, Superconductivity and normal-state transport in compressively strained $\text{La}_2\text{PrNi}_2\text{O}_7$ thin films (2025), [arXiv:2501.08022](https://arxiv.org/abs/2501.08022) [cond-mat.supr-con].
- [38] J. Shen, Y. Miao, Z. Ou, G. Zhou, Y. Chen, R. Luan, H. Sun, Z. Feng, X. Yong, P. Li, Y. Li, L. Xu, W. Lv, Z. Nie, H. Wang, H. Huang, Y.-J. Sun, Q.-K. Xue, Z. Chen, and J. He, Anomalous energy gap in superconducting $\text{La}_{2.85}\text{Pr}_{0.15}\text{Ni}_2\text{O}_7/\text{SrLaAlO}_4$ heterostructures (2025), [arXiv:2502.17831](https://arxiv.org/abs/2502.17831) [cond-mat.supr-con].
- [39] C. Yue, J.-J. Miao, H. Huang, Y. Hua, P. Li, Y. Li, G. Zhou, W. Lv, Q. Yang, H. Sun, Y.-J. Sun, J. Lin, Q.-K. Xue, Z. Chen, and W.-Q. Chen, Correlated electronic structures and unconventional superconductivity in bilayer nickelate heterostructures (2025), [arXiv:2501.06875](https://arxiv.org/abs/2501.06875) [cond-mat.str-el].
- [40] P. Li, G. Zhou, W. Lv, Y. Li, C. Yue, H. Huang, L. Xu, J. Shen, Y. Miao, W. Song, Z. Nie, Y. Chen, H. Wang, W. Chen, Y. Huang, Z.-H. Chen, T. Qian, J. Lin, J. He, Y.-J. Sun, Z. Chen, and Q.-K. Xue, Photoemission evidence for multi-orbital hole-doping in superconducting $\text{La}_{2.85}\text{Pr}_{0.15}\text{Ni}_2\text{O}_7/\text{SrLaAlO}_4$ interfaces (2025), [arXiv:2501.09255](https://arxiv.org/abs/2501.09255) [cond-mat.supr-con].
- [41] L. Bhatt, A. Y. Jiang, E. K. Ko, N. Schnitzer, G. A. Pan, D. F. Segedin, Y. Liu, Y. Yu, Y.-F. Zhao, E. A. Morales, C. M. Brooks, A. S. Botana, H. Y. Hwang, J. A. Mundy, D. A. Muller, and B. H. Goodge, Resolving structural origins for superconductivity in strain-engineered $\text{La}_3\text{Ni}_2\text{O}_7$ thin films (2025), [arXiv:2501.08204](https://arxiv.org/abs/2501.08204) [cond-mat.supr-con].
- [42] H. Wang, H. Huang, G. Zhou, W. Lv, C. Yue, L. Xu, X. Wu, Z. Nie, Y. Chen, Y.-J. Sun, W. Chen, H. Yuan, Z. Chen, and Q.-K. Xue, Electronic structures across the superconductor-insulator transition at $\text{La}_{2.85}\text{Pr}_{0.15}\text{Ni}_2\text{O}_7/\text{SrLaAlO}_4$ interfaces (2025), [arXiv:2502.18068](https://arxiv.org/abs/2502.18068) [cond-mat.supr-con].
- [43] X. Hu, W. Qiu, C.-Q. Chen, Z. Luo, and D.-X. Yao, Electronic structures and multi-orbital models of $\text{La}_3\text{Ni}_2\text{O}_7$ thin films (2025), [arXiv:2503.17223](https://arxiv.org/abs/2503.17223) [cond-mat.supr-con].
- [44] See supplemental material for s_{\pm} pairing via interlayer interaction in $\text{La}_{2.85}\text{Pr}_{0.15}\text{Ni}_2\text{O}_7$ thin films under ambient pressure.
- [45] J. Huang and T. Zhou, Interlayer pairing-induced partially gapped fermi surface in trilayer $\text{La}_4\text{Ni}_3\text{O}_{10}$ superconductors, *Phys. Rev. B* **110**, L060506 (2024).
- [46] Q. Qin, J. Wang, and Y. feng Yang, Frustrated superconductivity and intrinsic reduction of T_c in trilayer nickelate, *The Innovation Materials* **2**, 100102 (2024).
- [47] B. Ludbrook, G. Levy, P. Nigge, M. Zonno, M. Schneider, D. Dvorak, C. Veenstra, S. Zhdanovich, D. Wong, P. Dosanjh, C. Straßer, A. Stöhr, S. Forti, C. Ast, U. Starke, and A. Damascelli, Evidence for superconductivity in Li-decorated monolayer graphene, *Proc. Natl. Acad. Sci. U. S. A.* **112**, 11795–11799 (2015).
- [48] J. Chapman, Y. Su, C. A. Howard, D. Kundys, A. N. Grigorenko, F. Guinea, A. K. Geim, I. V. Grigorieva, and R. R. Nair, Superconductivity in Ca-doped graphene laminates, *Sci. Rep.* **6**, 23254 (2016).
- [49] S. Ichinokura, K. Sugawara, A. Takayama, T. Takahashi, and S. Hasegawa, Superconducting calcium-intercalated bilayer graphene, *ACS Nano* **10**, 2761 (2016).

Supplemental material for s_{\pm} pairing via interlayer interaction in $\text{La}_{2.85}\text{Pr}_{0.15}\text{Ni}_2\text{O}_7$ Thin Films under Ambient Pressure

S-1. TIGHT-BINDING MODEL

In the main text, we employed a two-orbital tight-binding bilayer model to describe the hole-doped $\text{La}_{2.85}\text{Pr}_{0.15}\text{Ni}_2\text{O}_7$ thin film. In Ref. [39], a smaller interlayer hopping constant for the d_{z^2} orbital was proposed, resulting in weaker bonding-anti-bonding splitting. This leads to larger γ and α Fermi surface pockets and the formation of an additional δ pocket near the Γ point.

However, recent ARPES experiments [40] measuring the normal-state Fermi surface revealed that the δ pocket does not form, and the γ and α pockets are smaller than predicted theoretically. These discrepancies suggest that the bonding-anti-bonding splitting may be stronger than previously estimated.

In our present work, we adopt a larger interlayer hopping constant to align with the ARPES results. Additionally, we adjust the chemical potential to ensure the electron filling matches the experimentally measured value of 1.28 [40]. The tight-binding parameters of our model are summarized in Table S1.

t_1^x	t_1^z	t_2^x	t_1^z	t_3^{xz}
-0.466	-0.126	0.062	-0.016	0.299
t_{\perp}^x	t_{\perp}^z	t_4^{xz}	ϵ^x	ϵ^z
0.001	-0.670	-0.032	1.140	0.455
t_4^x	t_4^z	t_5^x	t_5^z	t_5^{xz}
-0.064	-0.014	-0.015	-0.003	0.026
t_3^x	t_3^z			
-0.001	0.033			

TABLE S1.

In momentum space, the Hamiltonian can be expressed as $H = \sum_{\mathbf{k}} \Psi_{\mathbf{k}}^{\dagger} H(\mathbf{k}) \Psi_{\mathbf{k}}$, where the basis vector is defined as $\Psi_{\mathbf{k}}^{\dagger} = (c_{\mathbf{k}x\uparrow}^{1\dagger}, c_{\mathbf{k}z\uparrow}^{1\dagger}, c_{\mathbf{k}x\uparrow}^{2\dagger}, c_{\mathbf{k}z\uparrow}^{2\dagger}, c_{-\mathbf{k}x\downarrow}^1, c_{-\mathbf{k}z\downarrow}^1, c_{-\mathbf{k}x\downarrow}^2, c_{-\mathbf{k}z\downarrow}^2)$.

The Hamiltonian matrix $H(\mathbf{k})$ is an 8×8 matrix,

$$H(\mathbf{k}) = \begin{pmatrix} H_t(\mathbf{k}) & H_{\Delta}(\mathbf{k}) \\ H_{\Delta}^{\dagger}(\mathbf{k}) & -H_t(-\mathbf{k}) \end{pmatrix}, \quad (\text{S1})$$

where $H_t(\mathbf{k})$ represents the normal-state tight-binding Hamiltonian in a 4×4 matrix form,

$$H_t(\mathbf{k}) = \begin{pmatrix} H_A(\mathbf{k}) & H_{AB}(\mathbf{k}) \\ H_{AB}(\mathbf{k}) & H_A(\mathbf{k}) \end{pmatrix}. \quad (\text{S2})$$

The matrices $H_A(\mathbf{k})$ and $H_{AB}(\mathbf{k})$ are given by

$$H_A(\mathbf{k}) = \begin{pmatrix} T_k^x & V_k \\ V_k & T_k^z \end{pmatrix}, H_{AB}(\mathbf{k}) = \begin{pmatrix} T_k'^x & V_k' \\ V_k' & T_k'^z \end{pmatrix}. \quad (\text{S3})$$

The components are defined as

$$T_k^{x/z} = 2t_1^{x/z} (\cos \mathbf{k}_x + \cos \mathbf{k}_y) + 4t_2^{x/z} \cos \mathbf{k}_x \cos \mathbf{k}_y + 2t_4^{x/z} (\cos 2\mathbf{k}_x + \cos 2\mathbf{k}_y) + 2t_5^{x/z} (\cos 3\mathbf{k}_x + \cos 3\mathbf{k}_y) + \epsilon_{x/z}, \quad (\text{S4})$$

$$T_k'^{x/z} = t_{\perp}^{x/z} + 2t_3^{x/z} (\cos \mathbf{k}_x + \cos \mathbf{k}_y), \quad (\text{S5})$$

$$V_k = 2t_{3xz} (\cos \mathbf{k}_x - \cos \mathbf{k}_y), \quad (\text{S6})$$

$$V_k' = 2t_{4xz} (\cos \mathbf{k}_x - \cos \mathbf{k}_y). \quad (\text{S7})$$

The superconducting pairing part of the Hamiltonian, $H_{\Delta}(\mathbf{k})$, takes the form

$$H_{\Delta}(\mathbf{k}) = \begin{pmatrix} \Delta_{\mathbf{k}\parallel}^{1x} & 0 & \Delta_{\perp}^x & 0 \\ 0 & \Delta_{\mathbf{k}\parallel}^{1z} & 0 & \Delta_{\perp}^z \\ \Delta_{\perp}^x & 0 & \Delta_{\mathbf{k}\parallel}^{2x} & 0 \\ 0 & \Delta_{\perp}^z & 0 & \Delta_{\mathbf{k}\parallel}^{2z} \end{pmatrix}, \quad (\text{S8})$$

where $\Delta_{\mathbf{k}\parallel}^{l\tau} = 2\Delta_{\parallel}^{l\tau}(\cos \mathbf{k}_x + \cos \mathbf{k}_y)$. $\Delta_{\parallel}^{l\tau}$ is the intralayer order parameter obtained self-consistently.

S-2. ZERO ENERGY SPECTRAL FUNCTION IN THE SUPERCONDUCTING STATE WITH ONLY THE INTERLAYER PAIRING IN THE PRESENCE OF AN ADDITIONAL ELECTRONIC FIELD

In the main text, we investigate the effect of an additional electronic field on the interlayer pairing. Specifically, we consider an interlayer voltage $V_F = 0.2$ to demonstrate the emergence of Fermi arcs in the superconducting state [see Fig. 3(d) in the main text]. Here, we present additional numerical results for the zero-energy spectral function across different voltage values in Fig. S1.

Our calculations reveal that Fermi arcs first emerge at $V_F = 0.11$, coinciding with the initial separation of the α and β pockets. As V_F increases further, as shown in Fig. S1(b) and S1(c), the size of the Fermi arcs gradually expands. Additionally, the two arcs originating from the α and β pockets become increasingly well-separated with increasing voltage.

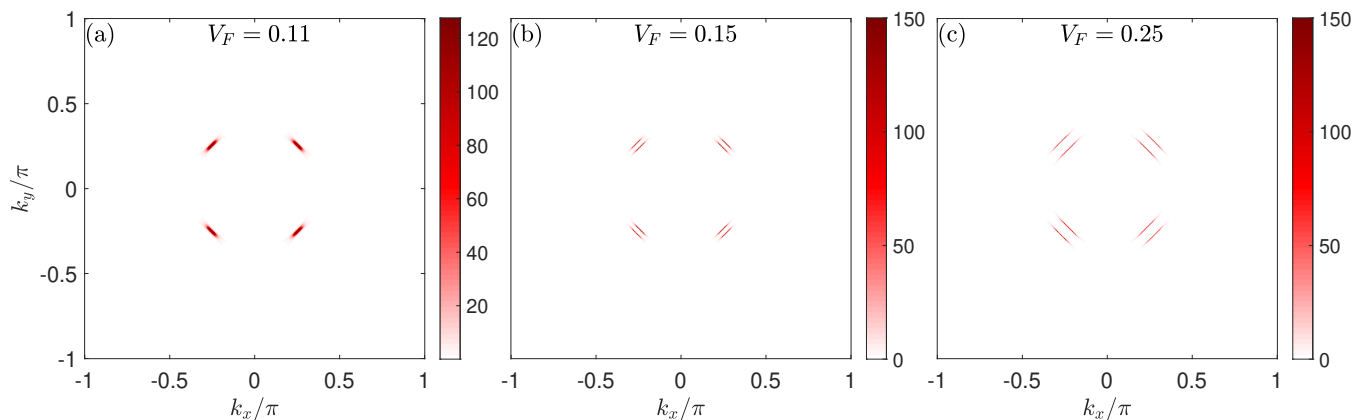


FIG. S1. Zero-energy spectral function in the superconducting state where only the interlayer pairing exists with (a) $V_F = 0.11$, (b) $V_F = 0.15$ and (c) $V_F = 0.25$.

S-3. NUMERICAL RESULTS WITH THE COEXISTENCE OF INTERLAYER PAIRING AND INTRALAYER PAIRING IN THE PRESENCE OF AN ADDITIONAL ELECTRONIC FIELD

In the main text, we presented numerical results for the case where only interlayer pairing exists in the presence of an electronic field. We now extend these results to the scenario where both intralayer and interlayer pairing coexist, with parameters $(V_{\perp}, V_{\parallel}) = (0.8, 0.6)$ in the presence of an electronic field. The numerical results for the intralayer and interlayer pairing order parameters are shown in Fig. S2.

Due to the breaking of layer equivalence by the applied field, the intralayer order parameters of the two layers are not identical. The intralayer order parameters exhibit weak dependence on the voltage V_F , while the interlayer order parameters decrease slightly with increasing V_F . Notably, even for a relatively large voltage of $V_F = 0.3$, the interlayer pairing order parameter for the d_{z^2} orbital remains dominant and significantly larger than pairing parameters in other channels.

The mean-field intralayer pairing order parameters are negative, as shown in Fig. S2, leading to negative superconducting gaps near the diagonal directions of the α and β pockets. The interlayer pairing generates a negative gap

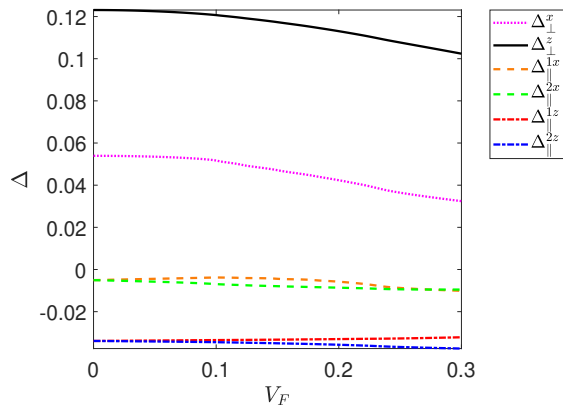


FIG. S2. Self-consistent results of interlayer and intralayer pairing order parameters as a function of voltage V_F .

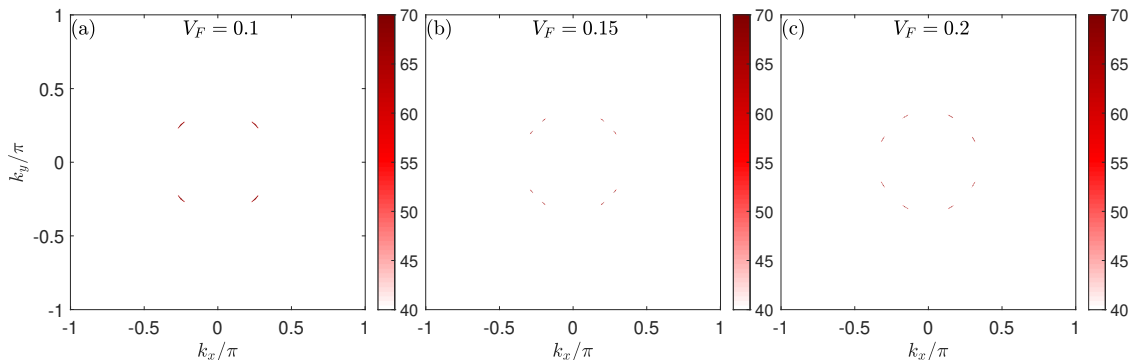


FIG. S3. Zero-energy spectral function in the superconducting state where interlayer and intralayer pairing coexist with (a) $V_F = 0.1$, (b) $V_F = 0.15$ and (c) $V_F = 0.2$.

along the β pocket and a positive gap along the α pocket. In the absence of an electronic field, interlayer pairing dominates, resulting in a nodeless energy gap across the entire Fermi surface. However, in the presence of an electronic field, as discussed in the main text, the gap induced by interlayer pairing near the diagonal directions of the α and β pockets is significantly suppressed. For the α pocket, the negative gap from intralayer pairing and the positive gap from interlayer pairing coexist, creating nodal points where these gaps cancel each other. For the β pocket, both interlayer and intralayer pairings contribute negative gaps, so no nodal points exist in this case.

We present the zero-energy spectral function for different values of V_F in Fig. S3. As shown, nodal points indeed appear in the α pocket for various V_F values, consistent with our analysis. The emergence of these nodal points in the α pocket with additional electronic field may serve as a useful experimental signature for probing the coexistence of interlayer and intralayer pairing.

The existence of nodal points can also be detected through the density of states (DOS) spectra, which are shown in Fig. S4. In Fig. S4(a), the absence of an electronic field results in a fully gapped system with a U-shaped gap. In contrast, Fig. S4(b) shows a V-shaped gap in the presence of an electronic field, indicating the presence of nodal points.

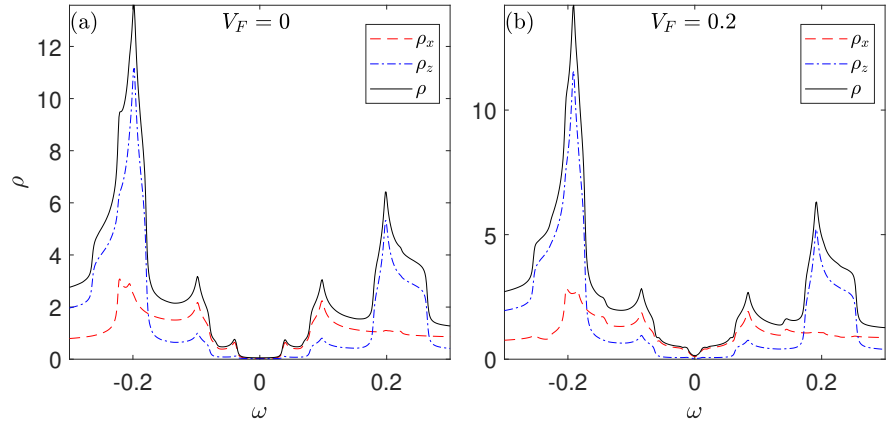


FIG. S4. DOS spectra in the superconducting states where interlayer and intralayer pairing coexist with (a) $V_F = 0$ and (b) $V_F = 0.2$.